Charge Transfer Between Ce and Fe During Cooling of an Aluminosilicate Melt: An In Situ XANES Investigation

Adrien Donatini, Peggy Georges, Tiphaine Fevre, Laurent Cormier, Daniel R. Neuville

Charge transfer between Ce and Fe during cooling of an aluminosilicate melt : An *In situ* XANES investigation.

Adrien Donatini[a,b,c], Peggy Georges[a], Tiphaine Fevre[a], Laurent Cormier[b], Daniel R. Neuville*[c]

a) Corning European Technology Center, 77210 Avon, France.

b) Sorbonne Université, Muséum National d'Histoire Naturelle, UMR CNRS 7590, IRD, Institut de Minéralogie, de Physique des Matériaux et de Cosmochimie, IMPMC, 75005 Paris, France

c) Géomatériaux, CNRS-IPGP, Université de Paris, 75005 Paris, France.

*Corresponding author: neuville@ipgp.fr

Abstract: Multivalent elements are often incorporated to silicate glasses to enhance specific properties to the final product. However, these properties strongly depend on the redox state of the multivalent elements. While the redox behavior of glasses containing a single multivalent element is well studied, research on the *in situ* interaction between multiple multivalent elements is scarce. In this study, *in situ* XANES spectroscopy was used to investigate the high temperature redox state of both Ce and Fe in an aluminosilicate melt. The results were compared to room temperature measurements. Our findings demonstrate that, at high temperature equilibrium, Ce and Fe act independently. However, upon cooling below 900°C, a charge transfer process occurs between the two elements as described by the reaction $Ce^{4+}+Fe^{2+}\rightarrow Ce^{3+}+Fe^{3+}$. The existence of such a charge transfer, observed even in melts doped with very low Ce and Fe amounts, could suggests that both elements are not randomly distributed in the melt. The intensity of the charge transfer process depends on the CeO_2/FeO ratio, with the element present in excess showing minimal change in redox state upon cooling. This explains the difference of room temperature redox state between samples.

1. Introduction

Multivalent elements are ubiquitous in the glass industry and in earth science, as they impart various properties such as color[1–3], luminescence[4,5] or even bioactivity[6,7]. Even though the room temperature redox state is important for the aforementioned properties, the high temperature redox state can influence the melt viscosity[8,9], the solubility limit of multivalent elements[10,11] or the thermal conductivity of the melt[12]. Several parameters influence the high temperature equilibrium redox state, including temperature, oxygen fugacity or glass composition[13–16].

Among the multivalent elements used in glass science, iron has been extensively studied as it is the most abundant multivalent element in natural glasses[9,14]. Fe is also a common impurity in the glass industry and is responsible of the greenish tint in window glass[17,18]. Conversely, cerium is used in high technology applications, such as optical fibers, where it is used alongside other rare-earth ions to reduce photodarkening[19,20] or in X-ray radiation shielding glasses[21,22].

The Fe-Ce pair is of particular interest in glass science as CeO_2 can be used as a decolorizer [23]. Indeed, Ce(IV) can oxidize Fe(II) to form the less colorful Fe(III) ion[24]. While the Fe-Ce interaction is desired at room temperature, it can be detrimental to the industrial process if it occurs in the molten state. The presence of Fe(II) in the silicate melt increases thermal conductivity and enhances energy transfer efficiency from the burners to the molten glass[12]. If Fe(II) is oxidized by Ce(IV) during melting, the energy efficiency of the furnace would decrease.

Additionally, CeO_2 is used as a fining agent in the glass industry[25]. When added to the raw materials and melted, CeO_2 is reduced and releases oxygen. This oxygen release allows existing bubbles to reach the critical size needed to escape the viscous melt. However, if Ce(IV) is reduced by Fe(II) at high temperature, the overall amount of oxygen released would decrease, reducing the fining efficiency and compromising the overall quality of the final product.

The Fe-Ce redox pair is also central to debates in Earth sciences. Given that Fe(II) is a very common ion in terrestrial conditions and Ce(IV) and Fe(II) cannot coexist at room temperature[24], it would be expected that Ce(IV) cannot be present in natural melts. However, results on the mineral-melt partitioning of Ce in ZrO_2 show the presence of Ce(IV) in natural melts[26–29].

In this study, we used *in situ* X-ray absorption near edge structure (XANES) spectroscopy at both Ce L_3-edge and Fe K-edge to investigate the high temperature redox states of Ce and Fe in glasses containing both elements. The goal is to compare the high temperature equilibrium redox states to those observed at room temperature. We closely monitored the redox evolution during quenching to understand how Ce and Fe interact with each another.

2. Experimental section

2.1 Glass synthesis. The base undoped glass used is the same as in a previous investigation[30]. The obtained glass was finely ground in an agate mortar and mixed with CeO_2 (99.9% Alfa Aesar) and/or Fe_2O_3 (99.9% trace metal basis, thermoscientific) to achieve molar concentrations ranging from 2 ‰ (per thousand) to 30 ‰ for CeO_2 and 0.5 ‰ to 30 ‰ for FeO. Note that the Fe concentration is given as FeO, even though the precursor used was Fe_2O_3.

The mixture was then melted four times at 1600°C, each time for two hours, using either a Pt or Pt-Au crucible (no difference was observed between the two types of crucibles). For samples containing more than 10‰ CeO_2, the temperature was slowly increased to 1600°C to prevent overflowing due to bubble release. After melting, the samples were quenched by dipping the bottom of the crucible into water.

The sample are labelled NASx for glasses containing only Ce, with x the molar concentration of CeO_2 expressed in ‰. Samples containing both FeO and CeO_2 are labelled NASFx_y, with x the molar concentration of CeO_2 expressed in ‰ and y the molar concentration of FeO expressed in ‰. As an example, sample NASF2_10 contains 2‰ CeO_2 and 10‰ FeO. The labelling NASF10_X series refers to all samples containing 10‰ CeO_2, regardless of the FeO concentration. The glass compositions were determined using EPMA (Electron Probe Micro-Analysis) and the results are reported in Table I.

Small amounts (<5 g) of NAS0.4 were remelted at 1350°C for 2 h under Ar(97.4%)/H_2(2.6%) reducing atmosphere to serve as a reduced reference for XANES measurements. This sample is labelled NAS0.4H2. Similarly, small amounts (<2 g) of NAS10 were remelted in a graphite crucible at 1500°C for 15 minutes to serve as a reduced reference for XANES measurements. This sample is labelled NAS10_GC.

2.2 EPMA. Electron Probe Micro-analysis (EPMA) measurements were performed on a Cameca SX-Five at the Camparis facility. A voltage of 25 kV and a beam size of 20 μm were used for all measurements. For Si, Na and Al, a current intensity of 4 nA and a counting time of 10 s were used, while a current intensity of 200 nA and a counting time of 20 s were applied to measure the low concentrations of Ce and Fe. The standards used for calibration were Albite (Na, Si), $(Mg,Fe)_3Al_2(SiO_4)_3$ (Al), FeS_2 (Fe) and a reference glass for Ce. At least ten measurements were performed for each composition, with the average values are reported in Table I.

2.3 Optical Absorption spectroscopy. Optical absorption spectra were recorded using a Perkin-Elmer® Lambda 1050 UV-Visible-NIR spectrophotometer in transmission mode in the range 4000 cm^{-1}-40000 cm^{-1}. Double-sided mirror-polished samples, with thickness ranging from 1000 to 200 microns, were used. A simple linear background was fitted to account for reflection. The spectra were corrected for sample thickness but were not normalized by total Ce or Fe concentration as Ce(III), Ce(IV), Fe(II) and Fe(III) are present in our samples and each redox state possesses distinct absorption bands (see section 3.1 for details).

2.4 XANES Ce L_3-edge. Ce L_3-edge XANES spectra were recorded on three different beamlines, ODE and LUCIA, located at the SOLEIL synchrotron facility (Saint-Aubin, France) and FAME (BM30B), located at the ESRF (Grenoble, France). For room temperature spectra, glass slices were polished to the appropriate thickness for measurements on ODE while powder was used on LUCIA (See section 2.6 for high temperature measurement).

Room temperature Ce L_3-edge XANES spectra acquired on the LUCIA beamline in fluorescence mode using a SDD (Silicon Drift Detector) detector[31]. A Si(111) double crystal monochromator was used for the incoming X-ray. The energy was calibrated at the first inflexion point of the Ti K-edge (4966 eV) using a Ti foil. To minimize photo-oxidation, a macro beam of 3x3 mm^2 was used. At least three scans, each lasting five minutes, were collected for all samples to evaluate possible photo-oxidation effects. For samples were photo-oxidation was suspected, ten spectra were recorded. Spectra were acquired in continuous mode (FLYSCAN) from 5680 eV to 5850 eV with a resolution of 0.2 eV and a duration of 300 ms per step. During the measurements, SOLEIL operated at 2.72 GeV and 500 mA.

Room temperature and *in situ* Ce L_3-edge XANES spectra recorded on the ODE beamline were obtained in dispersive transmission mode using a bent Si(111) monochromator[32]. Pixel to energy conversion was achieved through polynomial fitting using a CeO_2 reference. Spectra were acquired from 5670 eV to 5855 eV with a 0.2 eV resolution using a beam size of 100*100 μm^2, and collection times varied between 0.2 and 7 s.

During the measurements, SOLEIL operated at 2.72 GeV and 450 mA.

I*n situ* Ce L_3-edge XANES spectra recorded on the FAME beamline were collected in fluorescence mode with a multi-element solid state detector positioned at 90° relative to the incoming beam, the angle between the sample and the beam being 45°[33]. The incident photon energy was selected using a Si(220) double-crystal monochromator. Spectra were acquired step by step from 5680 eV to 5850 eV with a 0.2 eV resolution using a beam size of 200*80 μm^2. The acquisition time for a spectrum was typically 450 s. The measured flux at 5700 eV was about $3*10^{11}$ photons.s^{-1}. The energy was calibrated using a metallic Cr foil, setting the energy of the first maximum derivative of the absorption spectrum to 5989 eV. Energy calibration was ensured by regularly measuring the metallic Cr foil.

All XANES spectra were processed using the Larch software[34]. Pre-edge and post-edge regions were fitted by linear functions for normalization. Fitting was performed by calculating linear combinations of end-members, as described in section 3.2 for further details.

2.5 XANES Fe K-edge. *In situ* Fe K-edge XANES spectra recorded on the FAME beamline were collected in fluorescence mode with a multi-element solid state detector positioned at 90° relative to the incoming beam[33]. The incident photon energy was selected using a Si(220) double-crystal monochromator. Spectra were acquired step by step from 7080 eV to 7250 eV with a 0.2 eV resolution using a beam size of 200*80 μm^2. The acquisition time for a spectrum was typically 510 s. The flux measured at 7100 eV was about $4*10^{11}$ photons.s^{-1}. Energy calibration was performed using a metallic Fe foil, setting the energy of the first maximum of the derivative of the absorption spectrum to 7112 eV. Energy calibration was ensured by regularly measuring the metallic Fe foil.

Mineral references were measured as pellets.

All XANES spectra were processed using the Larch software[34]. Pre-edge and post edge regions were fitted by linear functions for normalization. Pre-edge fitting was done after removing the background from the white line using a constant + Lorentzian model. Two pseudo-Voigt functions were used to fit the pre-edge. Although constraining the parameter of these pseudo-Voigt functions can be useful to reduce the number of linked variables[35,36], it was not necessary for this study.

2.6 High temperature XANES experiments. High temperature experiments were conducted by loading glass powder into a 500 µm hole of 90Pt-10Ir wires[37]. The wires were heated by passing an electric current through them. Each wire was calibrated using the procedure detailed by Neuville and Mysen[25], see references therein for setup details. The temperature measurement error was conservatively set to $\pm$ 20°C.

Table I. Compositions (wt%) measured by EPMA as well as molar CeO_2/FeO ratio. Uncertainties on the last digit are given between brackets.

Sample	SiO_2	Al_2O_3	Na_2O	CeO_2	FeO[a]	Molar CeO_2/FeO ratio
NAS10	60.0 (8)	19.1 (4)	16.9 (4)	2.29 (2)	<0.005	**>200**
NAS2	61.6 (9)	19.7 (4)	17.1 (4)	0.50 (1)	0.038 (3)	**5.5**
NASF10_2	58,8 (7)	19,5 (2)	17,9 (3)	2,22 (1)	0,225 (4)	**4.0**
NASF2_05	60,8 (8)	19,7 (2)	18,3 (1)	0,510 (2)	0,067 (1)	**3.2**
NASF30_10	56,8 (6)	17,3 (3)	15,9 (3)	6,77 (7)	0,92 (2)	**3.1**
NASF10_10	58,8 (7)	19,1 (2)	17,4 (2)	2,75 (3)	1,06 (2)	**1.1**
NASF2_2	60,8 (9)	19,9 (2)	17,9 (3)	0,51 (1)	0,225 (4)	**0.9**
NASF10_30	56,9 (9)	18,9 (2)	16,8 (2)	2,17 (2)	3,19 (5)	**0.3**
NASF2_10	61,4 (9)	18,6 (3)	17,37 (9)	0,513 (7)	1,07 (2)	**0.2**
NASF0_1	62,0 (9)	18,9 (2)	17,8 (2)	<0.01	0,119 (3)	**<0.1**
NASF0_10	61,8 (8)	18,9 (2)	17,5 (2)	<0.01	1,02 (2)	**<0.01**

a) Total iron given as FeO.

3. Results

3.1 Optical absorption spectroscopy. Fe^{2+} and Fe^{3+} ions exhibit distinct absorption features in glass (Figure 1). The broad absorption band centered around 10000 cm^{-1} is characteristic of Fe^{2+}, whereas the three bands at 22400, 23700 and 26200 cm^{-1} are due to Fe^{3+}[18,38,39].

The absorption spectrum of the NASF0_10 sample (figure 1.D) shows absorption bands associated with valence states of iron present in the glass. This observation is consistent with the green sample color.

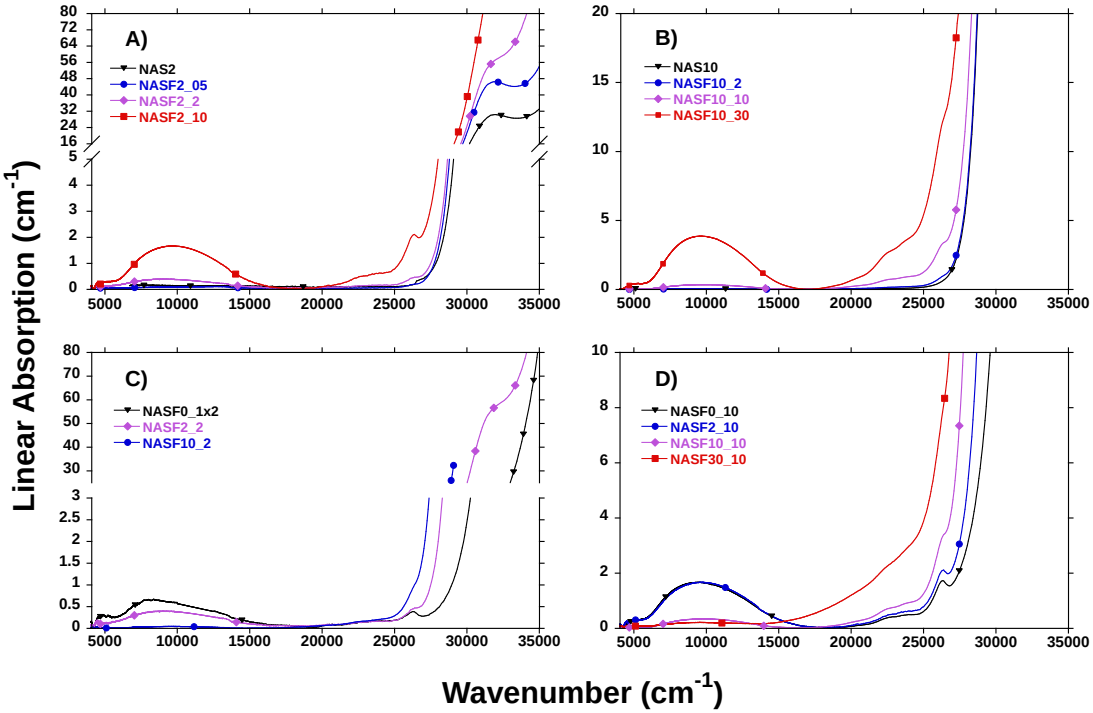

Figure 1. Optical absorption spectra of glasses doped with varying content of CeO_2 and FeO. A) NASF2_X glass series, B) NASF10_X glass series, C) NASFX_2 glass series with the absorption of NASF0_1 being multiplied by two to compare with the other samples. D) NASFX_10 glass series.

The shape of the Fe^{2+} absorption in NASF0_1 differs from NASF0_10 (figure 1.C), particularly with NASF0_1 showing relatively more intensity at lower wavenumbers, around 7000 cm^{-1}. This change in absorption shape suggests a variation in the local environment of Fe^{2+}, specifically its coordination, with changing concentration.

The detailed absorptions of Ce^{3+} and Ce^{4+} in the NAS glass have been previously reported[30]. Ce^{3+} show a prominent absorption band at 31464 cm^{-1} (Figure 1.A). However, this absorption is very intense and overlaps with the Oxygen-Metal Charge Transfer (OMCT) band associated with O-Fe^{3+} transitions. As a result, accurately measuring the absorption of Ce^{3+} becomes challenging when iron is also present. Therefore, this issue will not be discussed further in the present study.

The absorption spectra of NASF0_10 and NASF2_10 are nearly identical at low wavenumbers (figure 1.D), indicating that the addition of a small amount of CeO_2 does not alter the redox state of Fe when Fe is in excess. However, as the concentration of CeO_2 increases, the absorption band of Fe^{2+} decreases, becoming barely visible when CeO_2 is in excess. A similar trend can be observed in the NASFX_2 glass series (figure 1.C). Despite Fe^{2+} ions having a high absorption coefficient, their absorption is almost negligible for NASF10_2 (figure 1.B), suggesting that excess CeO_2 can fully oxidize Fe. This ability of CeO_2 to oxidize Fe is used in the glass industry to remove the blueish hue of the iron impurity in glasses[23,40].

3.2 Ce L_3-edge XANES. XANES spectroscopy at the Ce L_3-edge is sensitive to Ce oxidation state as the spectra for trivalent and tetravalent Ce differ significantly in the XANES region (figure 2). As shown in figure 2.B, Ce(III)PO_4 possesses a narrow white line with its maximum around 5727 eV, while Ce(IV)O_2 exhibits two distinct peaks at higher energies, 5731.5 and 5738 eV. Since both redox states have very different XANES spectra, a linear combination method is well suited to determine the redox state in our samples. This analytical approach has been successfully employed with data from the ODE and LUCIA in a previous investigation[30].

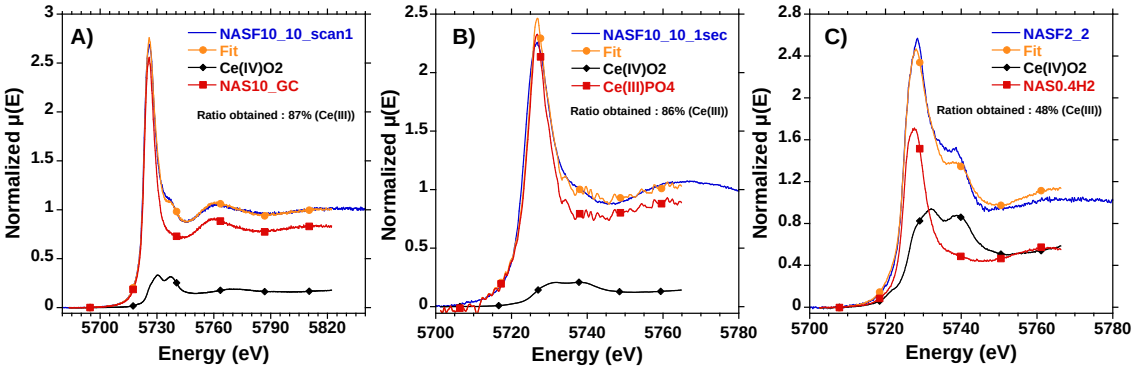

Figure 2 . Typical examples of linear combination fitting performed on the Ce-L_3 edge XANES spectra acquired on (A) LUCIA in fluorescence mode, (B) ODE in transmission mode and (C) FAME in fluorescence mode. See text for end-member used.

The choice of end-members for a linear combination analysis is important. Ideally, fully oxidized and reduced glass samples should be used. However, due to the low solubility and high potential of the Ce(III)/Ce(IV) redox couple, no fully oxidized sample could be synthetized[11,26,41]. We opted to use crystalline CeO_2 as the fully oxidized end-member rather than a partially oxidized glass. The deviation in the fit around 5735 eV can be attributed to the difference in the local environment of Ce in CeO_2 compared to that in the glass.

NAS10_GC was used as the reduced end-member for the LUCIA data, while crystalline $Ce(III)PO_4$ was used for the ODE data. As discussed in a previous study and as shown on figure 2, the choice of end-member and collection mode does not affect the determination of the redox state[30].

NAS0.4H2 was used as the reduced end-member for the FAME data. However, the spectra obtained from FAME were significantly more oxidized than those obtained from LUCIA or ODE for samples with similar CeO_2/FeO ratios. This difference is due to photo-oxidation of the sample under the X-ray beam[42]. Indeed, the surface flux at FAME was higher than at LUCIA, and the acquisition time was longer than at ODE, contributing to increased photo-oxidation effects. Therefore, reliable data at room temperature could not be obtained on the FAME beamline.

Photo-ionization processes are attenuated at higher temperatures[43] and no photo-oxidation occurred at temperatures exceeding the glass transition temperature, Tg (~600°C). An example on the FAME data is provided in supplementary figure S.1.

The data shown in Figure 2.A were acquired after 1 scan on the LUCIA beamline, while the data shown in figure 2.B were acquired in 1 second on the ODE beamline. Those correspond to the lowest exposure time toX-rays possible in order to minimize the impact of photo-oxidation of Ce under the beam. A more detailed investigation of the photo-oxidation effects on those two beamlines is presented in section 4.1.

3.3 Fe K-edge XANES. The treatment procedure applied to the Fe K-edge data was similar to that proposed by Wilke et al[36]. XANES data from mineral references were measured, and the centroid and area of their pre-edge are reported in the diagram below.

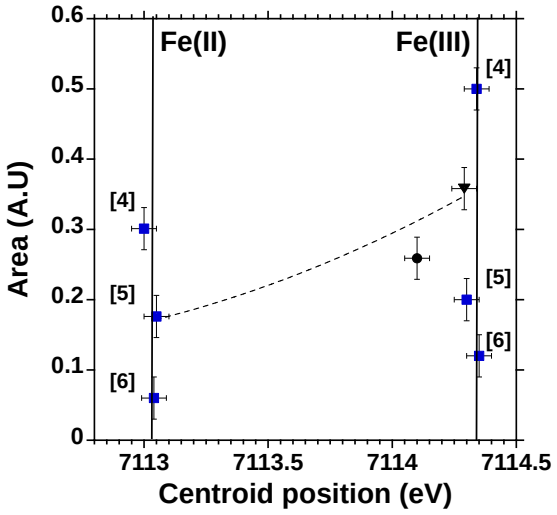

Figure 3. Pre-edge area and centroid of mineral references (blue squares) (full spectra can be found in figure S.2). NASF0_10 at 1200°C (black triangle), NASF0_10 at 1500°C (black circle). The dotted line shows the linear combination between the two end-members used in the study (see text for details).

The relative area of the pre-edge increases as the coordination decreases from octahedral to tetrahedral. Meanwhile, the centroid of the pre-edge increases when Fe is oxidized.

As shown in figure 3, the centroid of the NASF0_10 sample at 1200°C indicates that Fe is fully or nearly fully oxidized in the sample. This observation has already been reported in peralkaline systems[44] and is consistent with various models

[45,46]. However, when the temperature is increased to 1500°C, the centroid energy decreases, showing a partial reduction of iron. This decrease in centroid energy is also tied with a decrease in the pre-edge area, indicating that Fe(II) has a lower coordination number than Fe(III). This behavior was reported in several previous studies[14,47,48].

Fe(III) in our system exhibits an average coordination number between 4 and 5 (figure 3), which is not accurately modeled by any mineral reference. As such, for redox determination, the oxidized end-member used is the glass equilibrated at 1100°C or 1200°C, which is fully or almost fully oxidized, as shown in figure 3.

As no measurement were performed under reducing atmospheres, no fully reduced sample was obtained. Given the area measured at 1500°C, it is possible that the mean coordination number of Fe(II) is higher than 5. However, since no reference could model this behavior, a mean coordination number for Fe(II) of 5 will be considered, consistent with previous investigations[47–49]. This linear combination is represented by the dashed curve in figure 3.

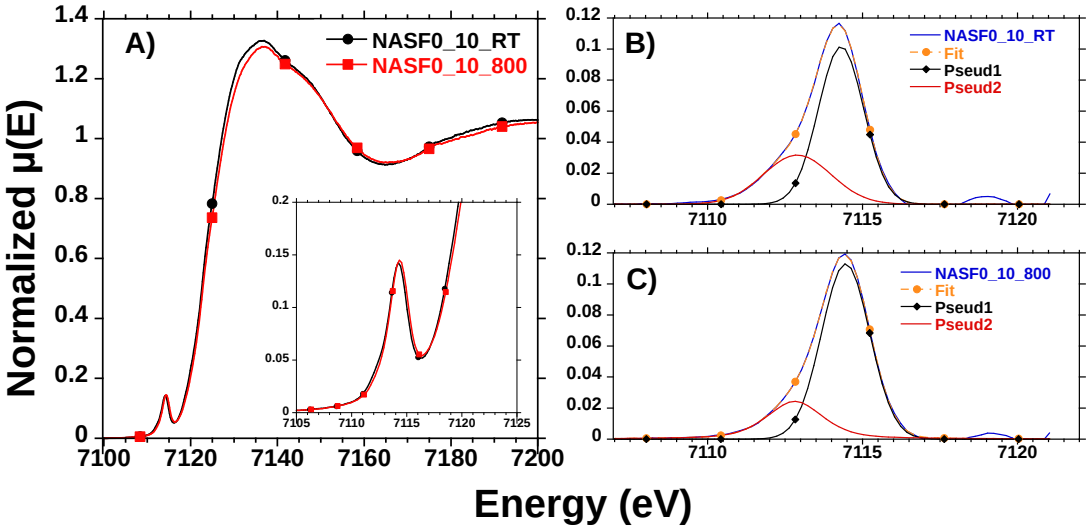

Figure 4. A) Fe K-edge of NASF0_10 sample measured on the FAME beamline at RT and 800°C. Decomposition of the pre-edge at RT B) and 800°C C). More details on the decomposition procedure can be found in the experimental section.

Fe is known to be photo-reduced by X-ray beams in glasses, especially at lower concentrations[43]. As the data were acquired on the FAME beamline, which has a high photon surface flux and acquisition times on the scale of 3-5 minutes, no reliable data could be obtained at room temperature. As shown in figure 4.A, when the temperature is increased from room temperature to 800°C (above Tg~600°C), the shoulder at lower energies in the pre-edge decreases in intensity (figure 4.B and 4.C). This highlights that photoreduction is no longer present at temperatures above Tg[43].

It is unlikely that the sample redox state is significantly influenced by diffusion during the first spectra acquisition at 800°C given that there is no change first spectra acquired at 800°C and the 16th one (see supplementary figure 3). Therefore, we will assume than the redox state measured at 800°C is the same as at room temperature, without any photo-reduction of the sample.

Under this assumption, the redox state of Fe at room temperature in sample NASF0_10 is 32% Fe(II). This is consistent with the results obtained from optical absorption spectroscopy, which shows the presence of both redox states.

4. Discussion

4.1 Kinetics of Ce photo-oxidation. We previously determined that photo-oxidation in glasses containing only Ce is too slow to affect measurements performed on the ODE and LUCIA beamlines (see supplementary information of a previous investigation)[30]. However, when Fe is also present in the system, Ce photo-oxidation appears to be faster and of a greater amplitude (figure 5).

The redox state measured on LUCIA is almost independent of the number of scans for sample NAS10. However, when Fe is added, the redox state changes between the first and second scan (figure 5.A**)**. Notably, the amplitude of the photo-oxidation could not be correlated with the amount of Fe in the glass.

The time resolution of the ODE beamline allows for a more precise study of photo-oxidation kinetics (figure 5.B). For a sample containing only Ce the phenomenon is well-modeled by a single exponential fit. Although it is ambitious to conclude that the process is purely exponential given the error bars, this assumption allows us to approximate the characteristic decay time of the photo-oxidation process, which is approximately 300s.

However, when Fe is present in the glass a simple exponential fit is insufficient to model the data. Instead, a bi-exponential fit was performed, highlighting two contributions. The slow contribution has a characteristic decay time of about 260 seconds, close to the one obtained for Fe-free sample. We attribute the slow contribution to the following reaction:

$$Ce^{3+} + h\upsilon \rightarrow Ce^{4+} + e' \quad \text{Eq 1.}$$

This mechanism implies the creation of an electronic defect in the glass network, which has a high activation energy, explaining the relatively slow kinetics.

The fast component of the bi-exponential fit has a characteristic decay time of about 30 seconds, which is one order of magnitude faster than the slow component. This fast component accounts for most of the photo-oxidation and is associated with a Ce-Fe interaction, following the reaction:

$$Fe^{3+} + Ce^{3+} + h\upsilon \rightarrow Ce^{4+} + Fe^{2+} \quad \text{Eq 2.}$$

This mechanism does not require the formation of any defect, resulting in a lower activation energy and a faster reaction time.

Such interactions between cerium and transition metals have been reported in literature, between Ce and Mn[50] and Ce and V[51]. Schreiber also reports a Ce-Fe proximity in silicate glasses using EPR[24]. The photo-oxidation data presented here shows that Ce and Fe are able to exchange an electron at room temperature.

Regardless, the first scan obtained on the LUCIA beamline and the first spectra obtained on the ODE beamline are not affected by photo-oxidation.

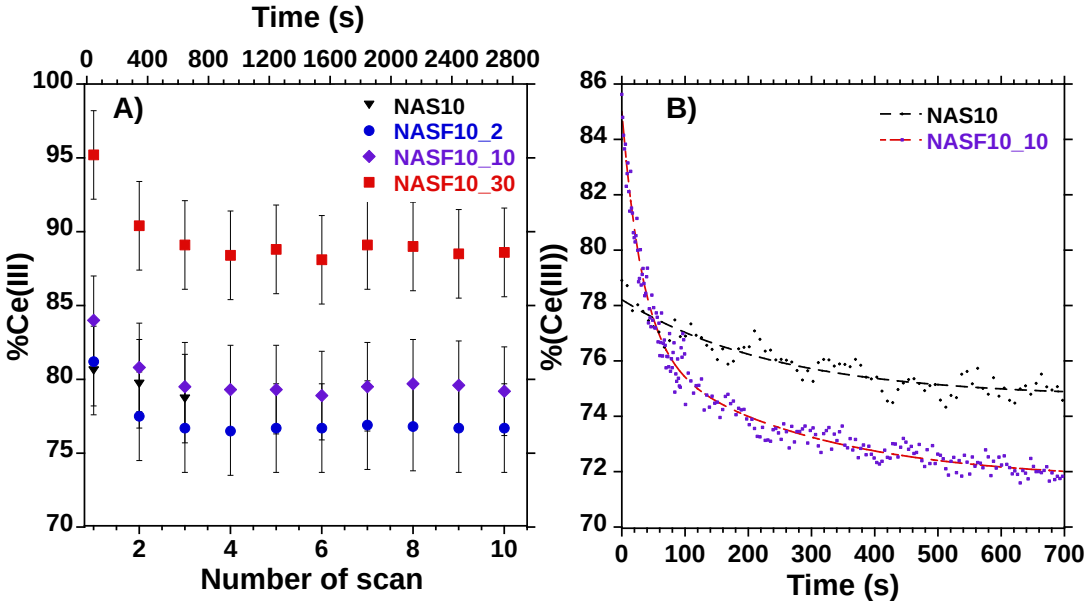

Figure 5 . A) Photo-oxidation kinetics measured on the LUCIA beamline for the NASF10_X series. Example of spectra can be found in supplementary figure 4 B) Photo-oxidation kinetics of samples NAS10 and NASF10_10 recorded on the ODE beamline. NAS10 is fitted with an exponential curve, NASF10_10 is fitted with a biexponential curve. Details of the fits, as well as example of spectra can be found in supplementary figure 4.

4.2 Room temperature interaction between Fe and Ce. Ce redox state measurements on the ODE and LUCIA beamlines yielded similar results as displayed in table II.

Table II. Ce redox state measured at room temperature on the ODE and LUCIA beamlines for the NASF10_X series.

	%Ce(III)	
Sample	LUCIA	ODE
NAS10	80±3%	80±3%
NASF10_2	81±3%	84±3%
NASF10_10	87±3%	86±3%
NASF10_30	95±3%	95±3%

For the remainder of the study, we will consider the LUCIA dataset for the values at room temperature of those glasses.

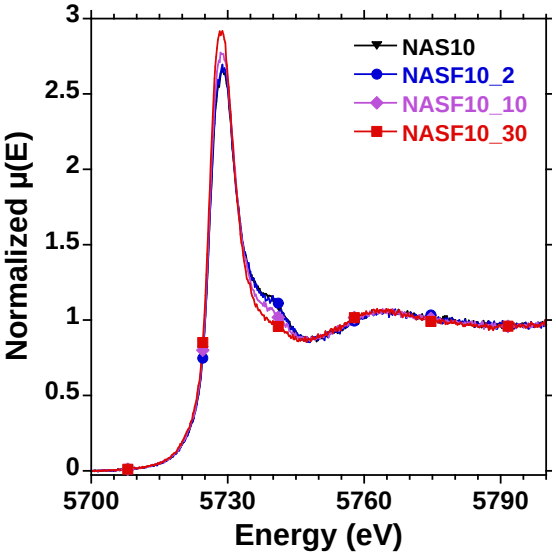

Figure 6. Ce L_3-edge XANES spectra of the NASF10_X sample series measured at room temperature on the LUCIA beamline.

Both Figure 6 and table II show that an increase in Fe concentration leads to a reduction of Ce. The extent of this reduction is of approximately 15% when Fe is in excess (CeO_2/FeO=0.3) (see Table II). This observation aligns with previous studies, as the expected reaction between both elements is as follows[24]:

$$Fe^{2+} + Ce^{4+} \rightarrow Fe^{3+} + Ce^{3+} \qquad \text{Eq 3.}$$

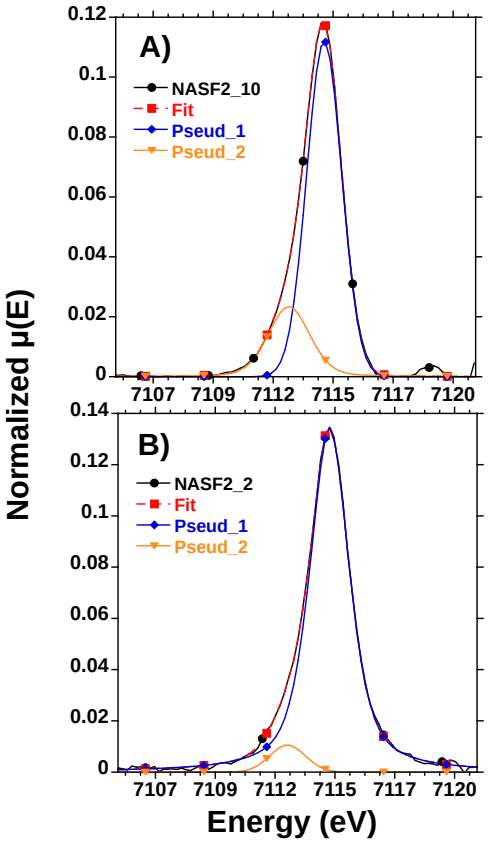

Figure 7. Baseline subtracted pre-edge fitting of the Fe K-edge of samples NASF2_10 and NASF2_2 at 800°C measured on the FAME beamline.

As shown in figure 7, the contribution at lower energies of the Fe K-edge XANES pre-edge is reduced when the Ce/Fe ratio increases. This results in an increase in centroid energy, indicating oxidation of the system. This shows that the presence of Ce oxidizes Fe at 800°C (see Table III).

Table III. Fe redox state measured 800°C immediately after the temperature change on the FAME beamline.

Sample	%Fe(II)
NASF0_10	32±7%
NASF2_10	33±7%
NASF2_2	14±7%
NASF2_05	0±7%

Fe is determined to be fully oxidized at 800°C when Ce is present is excess in the glass. The similarity of the results obtained at 800°C using XANES and at room temperature using optical absorption spectroscopy supports the assumption that the oxidation state of Fe immediately after heating to 800°C is the same as at room temperature.

The oxidation of Fe(II) by Ce(IV) presented in Table III, and the reduction of Ce(IV) by Fe(II) presented in Table II confirm that the reaction between the two elements follows equation 3.

Examining the results presented in Tables II and III, the redox state of the element in excess (Ce in NASF10_2 and Fe in NASF2_10) appears unaffected by the presence of the other element. This is also evident in figure 1.D, where the optical absorption spectra of NASF0_10 and NASF2_10 are nearly identical.

4.3 High temperature interaction between Fe and Ce. The redox state of Ce at room temperature was determined to be representative of its high temperature state for samples containing only Ce[30]. As the redox state of Ce at room temperature depends on the CeO_2/FeO ratio, it is reasonable to question whether the Ce-Fe interaction occurs in the molten state as well.

To measure the redox state *in situ*, samples were equilibrated in a 90Pt-10Ir wire microfurnace until no variation of the XANES spectra were observed. Due to the small sample volume, equilibrations times were relatively short, ranging from around 30 min at 1200°C to less than 5 min at 1500°C. The studied temperature range was chosen to prevent CeO_2 crystallization, with low

concentration samples showing no sign of crystallization at 1200°C, unlike their high concentration counterparts.

Figure 8.A shows the reduction of Ce with increasing temperature, which appears to be independent of the presence of Fe in the sample.

Neither the XANES measurements performed at the Ce L_3-edge on the NASF10_X series on ODE nor those on the NASF2_X series on FAME show a significant difference in the Ce redox state in presence of Fe (Figure 8 and Supplementary figure 5). Most importantly, the difference in redox state of about 15 % observed at room temperature is not observed at higher temperatures.

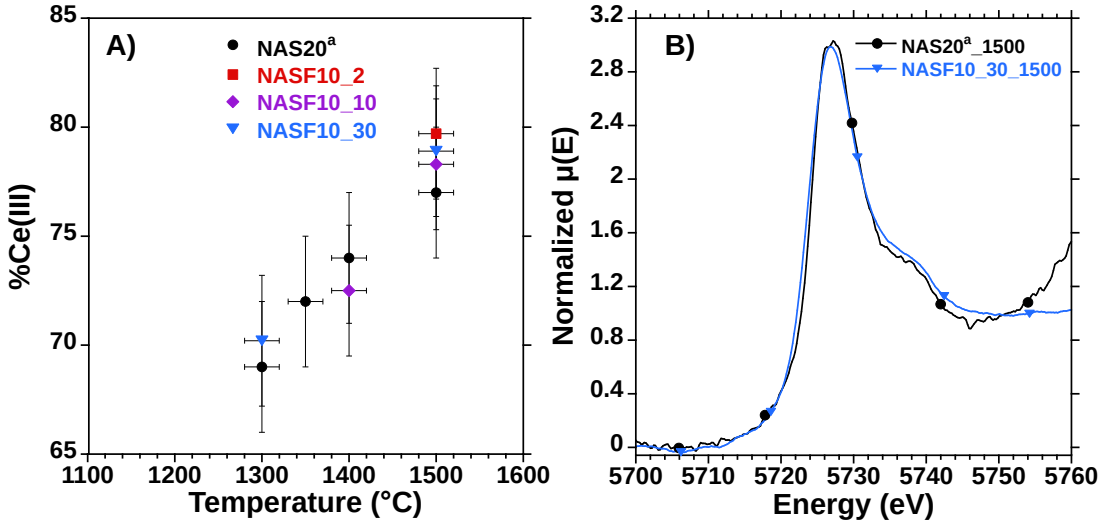

Figure 8. A) Evolution of the cerium redox state as a function of temperature measured *in situ* on the ODE beamline. B) Example of spectra. [a]The data for NAS20 was presented in a previous investigation[30]. See supplementary figure 5 for data acquired on the FAME beamline.

We can conclude that, at high temperature, the redox state of Ce is independent of the presence of Fe, even when Fe is present in excess (CeO_2/FeO<1). Similarly, the high temperature equilibrium of Fe seems independent of the presence of Ce, even when Ce is present in excess (CeO_2/FeO>1) (figure 9). Despite relatively significant error bars, the differences in high temperature redox states are smaller than those observed at 800°C.

We can also observe in figure 9.A that the oxidation states at 800°C of samples NASF0_10 and NASF2_10 are close to the redox state measured at high temperature. This shows that, upon quenching, the Fe redox state is frozen when Fe is either the only multivalent element or when it is present is excess. A similar conclusion was reached concerning Ce in a previous study were it was shown that diffusive processes are too slow to reequilibrate a sample during a quench[30].

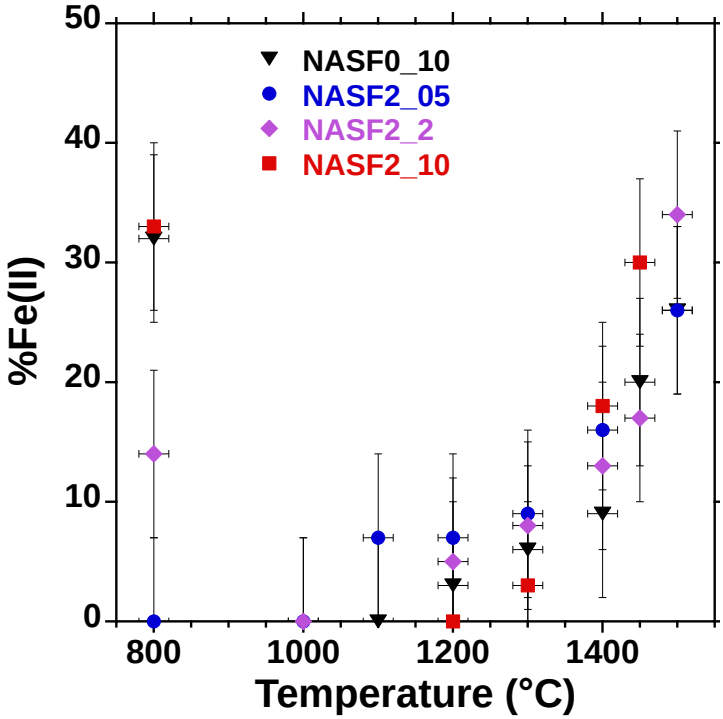

Figure 9. Evolution of the Fe redox state as a function of temperature measured on the FAME beamline. All points, except the one at 800°C, are at equilibrium (see section 3.3 for details). Example of spectra are available in supplementary figure 6.

Since the interaction between Ce and Fe observed at room temperature is not present at high temperature, it is necessary to investigate what occurs during the cooling of the sample.

4. Influence of Fe on the diffusive reequilibration of Ce. To investigate the difference between the high temperature equilibria and the room temperature redox state observed when both elements are present, we equilibrated samples at 1500°C before cooling them to 900°C. We then monitored the evolution of the Fe redox state over time. As 900°C is above the glass transition temperature (~600°C), no photo-oxidation due to the X-ray beam is expected to occur.

The results obtained show that the diffusive process responsible for Ce reequilibration is not influenced by the presence of Fe, even in excess (see figure 10). The diffusive nature of the mechanism is shown through the linear relationship between the evolution of the redox state and the square root of time (figure 10)[52].

This shows that the diffusive step of the mechanism, which is considered the limiting factor in the kinetics, is not affected by the presence of Fe. Therefore, the influence of Fe addition on the Ce redox state observed at room temperature is neither due to a different high temperature equilibrium nor to a change in diffusive process.

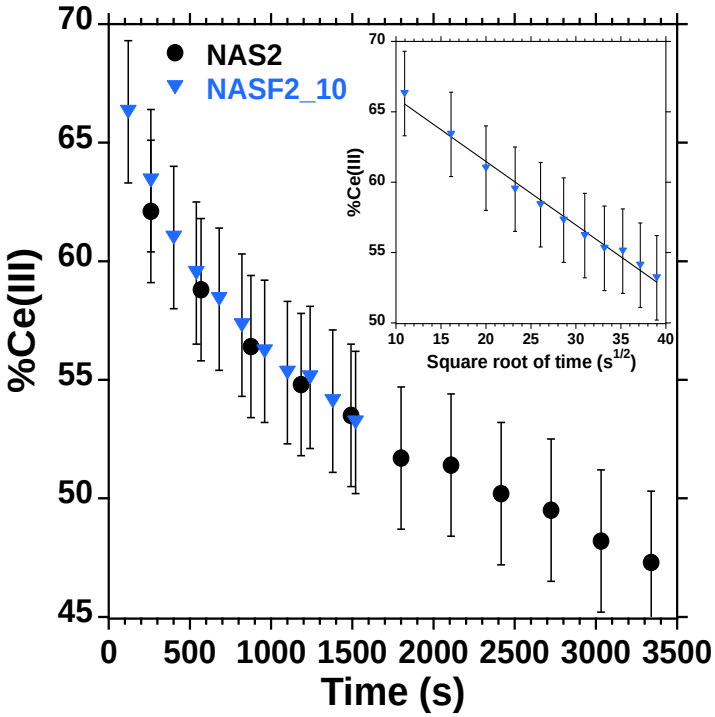

Figure 10. Evolution of Ce redox state in samples NAS2 and NASF2_10 measured on FAME as a function of time after a temperature change from 1500°C to 900°C. Insert shows the evolution of sample NASF2_10 as a function of the square root of time.

4.5 Ce-Fe charge transfer process. Since it is not feasible to measure the room temperature redox state of Ce due to photo-oxidation under the X-ray beam, we were unable to monitor the evolution of their redox state during quenching. Instead, we cooled the samples to the lowest temperature possible where no photo-oxidation is observed. This temperature is 700°C on the FAME beamline and 600°C on the ODE beamline. Figure 11 below illustrates the evolution of the redox state after the temperature change.

While 600°C is approximately the glass transition temperature of NASF10_30 (within the temperature error of the microfurnace), 700°C exceeds the glass transition temperature of sample NASF2_10 (Tg~600°C).

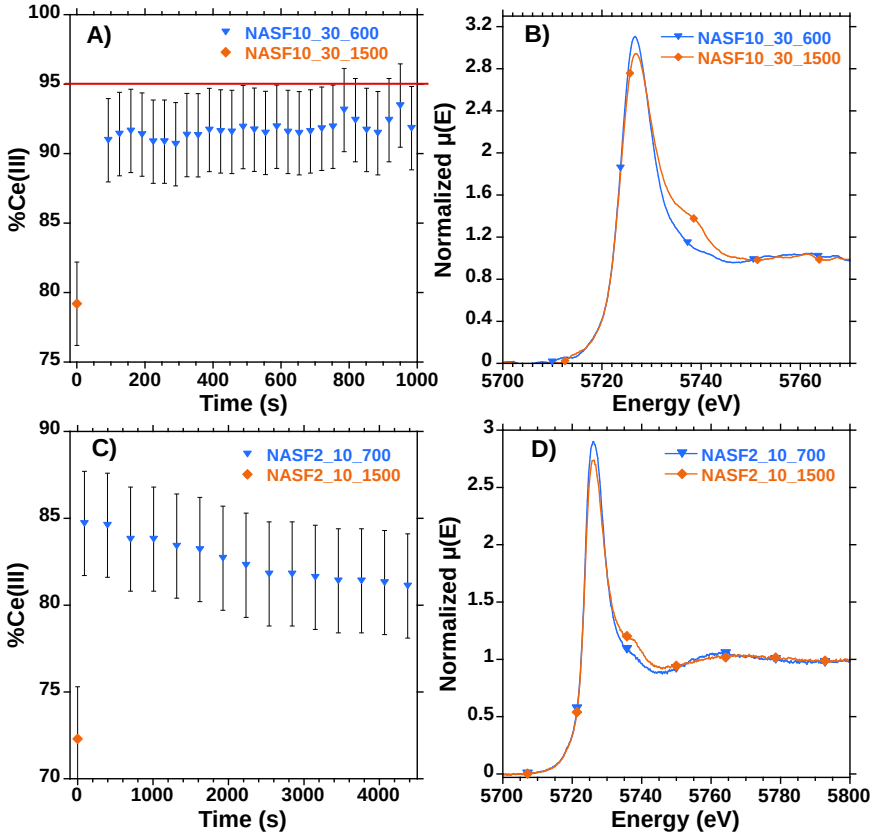

Figure 11. A) Evolution of Ce redox state for sample NASF10_30 measured on ODE after a temperature change from 1500°C to 600°C. Each point at 600°C corresponds to an average of 4 spectra. The red line shows the redox state measured at room temperature on the LUCIA beamline (Table II). B) Corresponding XANES spectra at the Ce L_3 edge, the spectra labelled 600°C is the first one acquired at this temperature. C) Evolution of Ce redox state for sample NASF2_10 measured on FAME after a temperature change from 1500°C to 700°C. D) Corresponding XANES spectra at the Ce L_3 edge, the spectra labelled 700°C is the first one acquired after the temperature change.

As shown in figures 11.C and 11.D, Ce undergoes reduction upon temperature decrease, and this reduction occurs too rapidly to be attributed to a diffusive process. Indeed, the slow reoxidation observed at 700°C is diffusion-limited and, even after an hour at this temperature, the Ce redox state changed by less than 5%. This abrupt change in redox state cannot be attributed to photo-oxidation of the sample as Ce is being reduced. Moreover, a decrease in temperature should shift the redox equilibrium towards Ce^{4+}, yet the opposite is observed.

Similar observations are noted with sample NASF10_30, where a reduction of similar amplitude is observed upon cooling (Figure 11.A). The resulting redox state after cooling is close to the one measured at room temperature on LUCIA. It is important to note that samples measured on LUCIA were quenched from 1600°C in a crucible and were not remelted in the 90Pt-10Ir microfurnace. This shows that our apparatus accurately reproduces the behavior of samples melted in traditional electrical furnaces.

Although similar experiments were not conducted at the Fe K-edge, the results present in Figure 9 suggest that the Fe redox state undergoes changes during quenching when Ce is present in the melt. Specifically, the high temperature equilibrium is independent (within the error bar) of the presence of Ce, whereas significant differences are observed in the redox state at 800°C between samples with and without Ce.

From this, we can conclude that the Ce-Fe interaction occurs during quenching through a charge transfer process following Eq. 3.

This process implies that Ce and Fe can exchange electrons during quenching, indicating that the two elements need to be spatially close to each other within the glass structure. As shown by the photo-oxidation kinetics presented in Figure 5, both elements can exchange electrons under X-ray excitation at room temperature. This underscores the proximity of Ce and Fe within the glass structure. A similar conclusion was reached by Schreiber et al.[24] who observed a change in Fe EPR spectra upon Ce addition.

Since the charge transfer process is observable even for sample NASF2_2, despite its relatively low multivalent doping, it would be worthwhile to calculate the atomic concentration of Ce and Fe ions in the glass.

Using the composition for sample NASF2_2 presented in Table I, as well as the density of the NAS2 glass (2.435 $g.cm^{-3}$) measured in a previous study[30], it is possible to estimate the Ce-Fe distance assuming a random distribution in the glass network.

We calculated the following concentrations for Fe and Ce ions:

Fe: $1.4*10^{19}$ at/cm^{-3}
Ce: $1.3*10^{19}$ at/cm^{-3}

No concentration quenching is seen in fluorescence spectroscopy at these concentrations for rare earths doped glasses[53–55]. This implies that, assuming a random distribution, Ce and Fe ions are too distant to interact with each other.

Using the concentrations we calculated earlier and assuming a random distribution, we can estimate the Ce-Fe distance to be comprised between 21 and 25 Å using a basic spheric model or comprised between 18 and 23 Å using the more accurate formula n°676 of Chandrashekhar[56] (see supplementary information).

Regardless of the model considered here, the Ce-Fe distance obtained is too large to explain the electron exchange during cooling or under X-ray excitation. This leads us to conclude that the Ce-Fe proximity does not follow a random distribution and, rather, that the two ions are located preferentially close to one another. This tendency of Ce to interact with transition metals has also been seen with Mn[57] or Ti[58], where the formation of Ce-O-Ti complexes explains the intense yellow coloration of Ce-Ti bearing glasses. This shows a relative proximity between Ce and transition metals at room temperature in glasses.

The existence of a charge transfer process between Ce and Fe has long been speculated to explain the mineral-melt partitioning of Ce in zircon[26,28,29]. Indeed, such a process can explain how Ce^{4+} and Fe^{2+} are able to react at room temperature while coexisting in geological settings.

A similar transfer has been successfully observed by Berry et al.[59] between Cr and Fe. This suggests that the Ce-Fe interaction is not unique and that analogous processes may occur with other multivalent elements.

4.6 Impact of the CeO_2/FeO ratio on the charge transfer amplitude. The reaction as described in Equation 3 implies a stoichiometric interaction between Ce and Fe. The CeO_2/FeO ratio should greatly influence the behavior of the charge transfer process, with the element present in lower concentration being more affected during quenching. This observation aligns with findings at room temperature as shown in Tables II and III.

Table IV and Figure 12 below display the evolution of the redox change due to the charge transfer process as a function of the CeO_2/FeO ratio. The equilibrium at 1500°C for sample NASF0_10 is used as the reference for all samples, primarily because not all glasses were measured at the same temperature (Figure 9). Moreover, the high temperature equilibrium of Fe was determined to be unaffected by the presence of Ce.

Table IV. Evolution of redox state of Ce and Fe due to the charge transfer process as a function of the CeO_2/FeO ratio

Sample	Measured CeO_2 /FeO	Delta redox Ce (%)[a] ±6%	Delta redox Fe (%)[b] ±14%
NAS10	>200	-1	
NASF10_2	4.0	-2	
NASF2_05	3.2		-32
NASF30_10	3.1	-1	
NASF10_10	1.1	10	
NASF2_2	0.9	7	-18
NASF10_30	0.3	13	
NASF2_10	0.2	13	1
NASF0_10	<0.01		0

[a] The redox difference is calculated between the equilibrium at 1500°C and the redox measured right after the cooling to 600 or 700°C (Figure 11).
[b] The redox difference is calculated between the equilibrium at 1500°C for sample NASF0_10 and the redox measured at 800°C (Figure 9.A), see text for details.

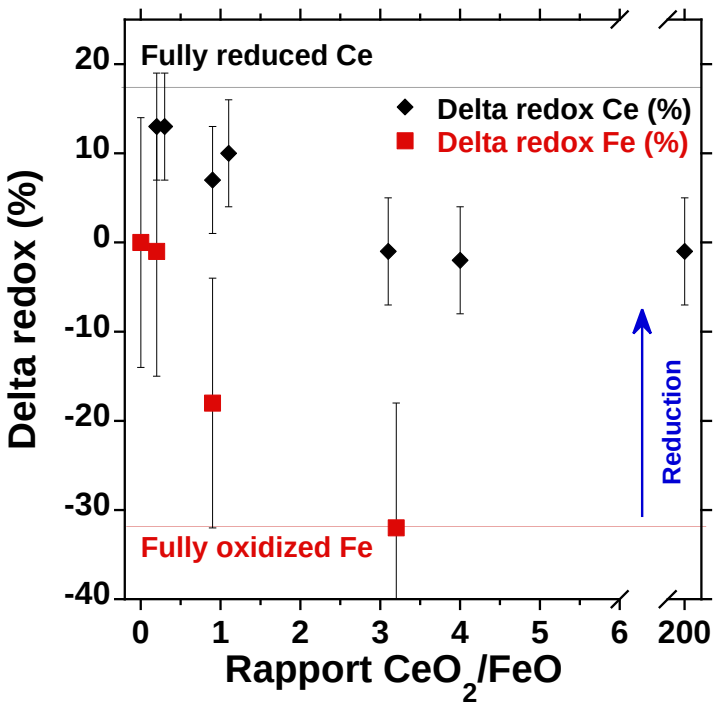

Figure 12. Evolution of cerium (black diamonds) and iron (red squares) redox state during quenching as a function of measured CeO_2/FeO ratio.

When Fe is present in excess in the glass (CeO_2/FeO<1), Ce tends to be fully reduced while the redox state of Fe remains unchanged. Conversely, when Ce is present in excess (CeO_2/FeO>1), Fe tends to be fully oxidized while the redox state of Ce remains unchanged. When the CeO_2/FeO ratio decreases, the Ce reduction upon cooling becomes more important. Similarly, when the CeO_2/FeO ratio increases, the Fe oxidation upon cooling becomes more important. (Figure 12). It appears that when the two elements are present in similar concentrations, both their redox states are influenced by the charge transfer process.

This result implies that a trace multivalent element does not influence the redox state of multivalent elements present in higher concentrations. This is particularly noteworthy in the case of Fe which is always present in the glass as an impurity.

.

When comparing the oxidation of Fe and the reduction of Ce during quenching, it appears that Fe is more oxidized than Ce is reduced (Table IV). For example, samples NASF30_10 and NASF10_2 both have similar CeO_2/FeO ratios, however, upon cooling Ce redox state in NASF10_2, Fe gets oxidized by 32%, given the CeO_2/FeO ratio a corresponding Ce reduction of around 10% is expected. However, when the same experiment is performed with sample NASF30_10, Ce redox state doesn't change upon cooling. There is an apparent discrepancy between how much Fe is oxidized and how much Ce is reduced.

This seems contradictory considering that Equation 3 supposes a stoichiometric reaction between Ce^{4+} and Fe^{2+}. Our explanation is that there might be a mild surface reoxidation when the cooling occurs.

4.7 Threshold temperature for the charge transfer process. While the charge transfer process is clearly evident when the sample is cooled from 1500°C to 700°C (Figure 11), no such charge transfer is observed when the final temperature is 900°C (Figure 10). This suggests that the interaction between Ce and Fe occurs only when the temperature is sufficiently low[60].

In a recent review, Cooper[61] highlighted the following model: at high temperature, three redox couples are active, Ce(III)/Ce(IV), Fe(II)/Fe(III) and O(-II)/O(0). At equilibrium, the potential of each redox couple is equal. Given that the oxygen couple is present in the highest concentration, oxygen governs the equilibrium for both Ce and Fe. This explains why the redox states of Ce and Fe remain independent at high temperatures. The sample is considered as an open system interacting with the atmosphere.

Conversely, upon quenching, the glass becomes effectively isolated from the atmosphere, as diffusion slows down or encounters energetic barriers. The glass can then be considered as a closed system[61], no longer in equilibrium with the atmosphere. In this scenario, only two redox couples are active, Ce(III)/Ce(IV) and Fe(II)/Fe(III), allowing them to interact with each other.

This simple open/close system model explains why multivalent elements interact upon quenching and not at high temperature. However, the transition from open to closed system depends on the chemical diffusion of oxygen in the system. When oxygen diffusion becomes sufficiently slow, multivalent elements begin to interact. We can define three distinct regimes[60,61]: (i) The open regime, where the sample is equilibrated with air. (ii) The closed active regime, where the sample is isolated from the outside atmosphere. In this regime, multivalent ions in the glass have sufficient mobility to exchange electrons. (iii) The closed inactive regime, where ionic mobility is too low to allow any interaction between Ce and Fe. Given the apparent proximity between Ce and Fe, the existence of the close inactive regime is questionable in our case.

In this three-regime model, the charge transfer process can only occur during the closed active regime, leading to a metastable state when the temperature is subsequently decreased to the closed inactive regime.

Our data partly confirms this representation, as no interaction between Ce and Fe is seen at high temperature. We also confirm that the interaction between Ce and Fe occurs too rapidly to be limited by diffusion.

However, our data does not align with the three-regime model on every aspect. Upon cooling to 700°C (Figure 11.C), a charge transfer process occurs during the cooling, followed by a slow diffusive reequilibration. This shows that both phenomena can occur at the same temperature. However, upon cooling to 900°C (Figure 10), no charge transfer is visible before the diffusion process begins. One would expect Ce and Fe to interact before diffusion slowly reequilibrates the melt, especially because the diffusion remains too slow, even at 900°C.

Our results suggests that the sample's temperature needs to be decreased below a certain threshold for Ce and Fe to interact. A similar behavior was observed between Ce and Sb[62] or As and Mn[60], where the oxidoreduction reaction varies with temperature.

This temperature threshold is not included in the three-regime model described previously which only considers oxygen diffusion. This observation has significant implications because the threshold temperature is mostly dependent of the couple of elements studied whereas oxygen diffusivity is mostly influenced by glass viscosity and composition.

It is also possible to consider the charge transfer process not as an electron exchange but as an oxygen exchange. The following equation gives an example of such a reaction with assumed coordinences for Fe and Ce:

$$FeO_5^{8-} + CeO_8^{12-} \rightleftharpoons FeO_4^{5-} + CeO_9^{15-} \qquad Eq4$$

An oxygen exchange requires local structural rearrangements compared to a simple electron exchange described by Eq3. Therefore, it should theoretically be possible to quench the system fast enough to prevent the charge transfer process

The presence of two multivalent elements allows for them to change coordinence upon quenching

Such a reaction requires more important structural rearrangements than Eq3.

V. Conclusion

Using *in situ* XANES spectroscopy at both Ce L_3-edge and Fe K edge, we observed that the two elements interact in aluminosilicate glasses through the following oxidoreduction reaction.

$$Fe^{2+} + Ce^{4+} \rightarrow Fe^{3+} + Ce^{3+}$$

This reaction occurs even if both elements are present in relatively low concentrations, showing that their relative distribution is not random.

In situ measurements revealed that the high temperature equilibria of Ce and Fe are independent of each other, as oxygen sets the redox potential at high temperatures.

Upon cooling of the glass, a charge transfer process occurs between Ce and Fe, which determines the redox state observed at room temperature. The extent of this charge transfer process depends on the ratio between both elements. The element present in excess undergoes minimal changes in redox state, while a more pronounced change is observed for the element present in deficit. This finding is significant for industrial applications, indicating that Fe impurities do not influence the redox state of intentionally added multivalent elements in the melt. The independence of multivalent elements at equilibrium at high temperatures also simplifies processes such as glass fining inside furnaces.

The charge transfer process becomes only visible when the glass is cooled down below a certain temperature threshold, typically between 700 and 900°C. While the exact temperature is not critical for the purpose of quenching to room temperature, it can be significant for thermal treatment applications.

Supplementary Material

Ce L_3-edge XANES spectra of sample NASF2_2 measured on the FAME beamline at different temperature (PDF).

Acknowledgments

We thank SOLEIL (Gif-sur-Yvette, France) for provision of synchrotron facilities (project numbers 20221616 and 20221459) as well as Lucie Nataf and Nicolas Trcera for their help on the ODE and Lucia beamline respectively. We acknowledge the European Synchrotron Radiation Facility (ERSF) for provision of synchrotron radiation facilities (project number 20230331) and we would like to thank Isabelle Kieffer for assistance in using beamline CRG-FAME BM30 beamline.
This work was supported by ANRT, under the CIFRE Contract 2021/0986 and by Corning SAS.

Author declarations section

Conflict of interest

The authors have no conflict of interest to disclose.

Author contributions

Adrien Donatini: Investigation (lead); Visualization (lead); Writing/Original draft preparation (lead); Writing/Review & Editing (equal). **Peggy Georges:** Funding Acquisition (lead); Conceptualization (equal); Resources (equal); Supervision (equal); Writing/Review & Editing (equal). **Tiphaine Fevre:** Conceptualization (equal); Supervision (equal); Writing/Review & Editing (equal). **Laurent Cormier:** Conceptualization (equal); Resources (equal); Supervision (equal); Writing/Review & Editing (equal). **Daniel Neuville:** Conceptualization (equal); Resources (equal); Supervision (equal); Writing/Review & Editing (equal).

Data availability statement

The data that support the findings of this study are available from the corresponding author upon reasonable request.

REFERENCES

(1) Thiemsorn, W.; Keowkamnerd, K.; Suwannathada, P.; Hessenkemper, H.; Phanichaphant, S. Redox Ratio and Optical Absorption of Polyvalent Ions in Industrial Glasses. *Bull Mater Sci* **2007**, *30* (5), 487–495. https://doi.org/10.1007/s12034-007-0077-7.

(2) Calas, G.; Galoisy, L.; Cormier, L. The Color of Glass. In *Encyclopedia of Glass Science, Technology, History, and Culture*; Richet, P., Conradt, R., Takada, A., Dyon, J., Eds.; Wiley, 2021; pp 677–691. https://doi.org/10.1002/9781118801017.ch6.2.

(3) Rossano, S.; Khomenko, V.; Bedidi, A.; Muller, C.; Loisel, C.; Ferrand, J.; Sarrasin, L.; Bertin, A. Glass Colourations Caused by Mn-Fe Redox Pair : Application to Ancient Glass Technology. *Journal of Non-Crystalline Solids* **2022**, *594*, 121710. https://doi.org/10.1016/j.jnoncrysol.2022.121710.

(4) Abdel-Hameed, S. A. M.; Hamdy, Y. M.; Sadek, H. E. H. Characterization and Luminescence Properties of Mn-Doped Zinc Borosilicate Glasses and Glass-Ceramics. *Silicon* **2019**, *11* (3), 1185–1192. https://doi.org/10.1007/s12633-017-9685-z.

(5) Song, H.; Lu, S.; E, S.; Gao, R.; Zhang, J.; Chen, B.; Xia, H.; Zhang, J.; Ni, Q. Fluorescence Properties of Divalent and Trivalent Europium Ions in Aluminosilicate Glasses. *Journal of Applied Physics* **2002**, *91* (5), 2959–2964. https://doi.org/10.1063/1.1450052.

(6) Kargozar, S.; Baino, F.; Hamzehlou, S.; Hill, R. G.; Mozafari, M. Bioactive Glasses Entering the Mainstream. *Drug Discovery Today* **2018**, *23* (10), 1700–1704. https://doi.org/10.1016/j.drudis.2018.05.027.

(7) Miola, M.; Brovarone, C. V.; Maina, G.; Rossi, F.; Bergandi, L.; Ghigo, D.; Saracino, S.; Maggiora, M.; Canuto, R. A.; Muzio, G.; Vernè, E. In Vitro Study of Manganese-Doped Bioactive Glasses for Bone Regeneration. *Materials Science and Engineering: C* **2014**, *38*, 107–118. https://doi.org/10.1016/j.msec.2014.01.045.

(8) Osugi, T.; Sukenaga, S.; Inatomi, Y.; Gonda, Y.; Saito, N.; Nakashima, K. Effect of Oxidation State of Iron Ions on the Viscosity of Alkali Silicate Melts. *ISIJ Int.* **2013**, *53* (2), 185–190. https://doi.org/10.2355/isijinternational.53.185.

(9) Di Genova, D.; Vasseur, J.; Hess, K.-U.; Neuville, D. R.; Dingwell, D. B. Effect of Oxygen Fugacity on the Glass Transition, Viscosity and Structure of Silica- and Iron-Rich Magmatic Melts. *Journal of Non-Crystalline Solids* **2017**, *470*, 78–85. https://doi.org/10.1016/j.jnoncrysol.2017.05.013.

(10) Farges, F.; Linnen, R. L.; Brown, G. E. Redox and Speciation of Tin in Hydrous Silicate Glasses: A Comparision with Nb, Ta, Mo and W. *The Canadian Mineralogist* **2006**, *44* (3), 795–810. https://doi.org/10.2113/gscanmin.44.3.795.

(11) Cachia, J.-N.; Deschanels, X.; Den Auwer, C.; Pinet, O.; Phalippou, J.; Hennig, C.; Scheinost, A. Enhancing Cerium and Plutonium Solubility by Reduction in Borosilicate Glass. *Journal of Nuclear Materials* **2006**, *352* (1–3), 182–189. https://doi.org/10.1016/j.jnucmat.2006.02.052.

(12) Hubert, M.; Faber, A. J.; Sesigur, H.; Akmaz, F.; Kahl, S.-R.; Alejandro, E.; Maehara, T. Impact of Redox in Industrial Glass Melting and Importance of Redox Control. In *Ceramic Engineering and Science Proceedings*; Sundaram, S. K., Ed.; John Wiley & Sons, Inc.: Hoboken, NJ, USA, 2017; pp 113–128. https://doi.org/10.1002/9781119417507.ch11.
(13) Wiedenroth, A.; Rüssel, C. The Effect of MgO on the Thermodynamics of the Fe2+/Fe3+-Redox Equilibrium and the Incorporation of Iron in Soda-Magnesia-Aluminosilicate Melts. *Journal of Non-Crystalline Solids* **2003**, *320* (1), 238–245. https://doi.org/10.1016/S0022-3093(03)00076-0.
(14) Le Losq, C.; Moretti, R.; Oppenheimer, C.; Baudelet, F.; Neuville, D. R. In Situ XANES Study of the Influence of Varying Temperature and Oxygen Fugacity on Iron Oxidation State and Coordination in a Phonolitic Melt. *Contrib Mineral Petrol* **2020**, *175* (7), 64. https://doi.org/10.1007/s00410-020-01701-4.
(15) Rüssel, C.; von der Gönna, G. The Electrochemical Series of Elements in the Na2O Á 2SiO2 Glass Melt. *C. R* **1999**.
(16) Pinet, O.; Phalippou, J.; Di Nardo, C. Modeling the Redox Equilibrium of the Ce4+/Ce3+ Couple in Silicate Glass by Voltammetry. *Journal of Non-Crystalline Solids* **2006**, *352* (50–51), 5382–5390. https://doi.org/10.1016/j.jnoncrysol.2006.08.034.
(17) Thomsen, S. V.; Landa, K. A.; Landa, L. M.; Hulme, R. Clear Glass Composition. US 7,560,402 B2, July 14, 2009.
(18) Vercamer, V.; Lelong, G.; Hijiya, H.; Kondo, Y.; Galoisy, L.; Calas, G. Diluted Fe 3+ in Silicate Glasses: Structural Effects of Fe-Redox State and Matrix Composition. An Optical Absorption and X-Band/Q-Band EPR Study. *Journal of Non-Crystalline Solids* **2015**, *428*, 138–145. https://doi.org/10.1016/j.jnoncrysol.2015.08.010.
(19) Engholm, M.; Jelger, P.; Laurell, F.; Norin, L. Improved Photodarkening Resistivity in Ytterbium-Doped Fiber Lasers by Cerium Codoping. *Opt. Lett.* **2009**, *34* (8), 1285. https://doi.org/10.1364/OL.34.001285.
(20) Jetschke, S.; Unger, S.; Schwuchow, A.; Leich, M.; Jäger, M. Role of Ce in Yb/Al Laser Fibers: Prevention of Photodarkening and Thermal Effects. *Opt. Express* **2016**, *24* (12), 13009. https://doi.org/10.1364/OE.24.013009.
(21) Wang, Z.; Cheng, L. Structural Evolution of CeO_2-Doped Alkali Boroaluminosilicate Glass and the Correlation with Physical Properties Based on a Revised Structural Parameter Analysis. *RSC Adv.* **2016**, *6* (7), 5456–5465. https://doi.org/10.1039/C5RA20487A.
(22) Yılmaz, D.; Aktaş, B.; Yalçın, Ş.; Albaşkara, M. Erbium Oxide and Cerium Oxide-Doped Borosilicate Glasses as Radiation Shielding Material. *Radiation Effects and Defects in Solids* **2020**, *175* (5–6), 458–471. https://doi.org/10.1080/10420150.2019.1674301.
(23) Vargin, V. V.; Osadchaya, G. A. Cerium Dioxide as a Fining Agent and Decolorizer for Glass. *Glass Ceram* **1960**, *17* (2), 78–82. https://doi.org/10.1007/BF00692388.
(24) Schreiber, H. D.; Lauer, H. V.; Thanyasiri, T. Oxidation-Reduction Equilibria of Iron and Cerium in Silicate Glasses: Individual Redox Potentials and Mutual Interactions. *Journal of Non-Crystalline Solids* **1980**, *38–39*, 785–790. https://doi.org/10.1016/0022-3093(80)90532-3.
(25) Pereira, L.; Podda, O.; Fayard, B.; Laplace, A.; Pigeonneau, F. Experimental Study of Bubble Formation in a Glass-Forming Liquid Doped with Cerium Oxide. *Journal of the American Ceramic Society* **2020**, *103* (4), 2453–2462. https://doi.org/10.1111/jace.16950.
(26) Burnham, A. D.; Berry, A. J. The Effect of Oxygen Fugacity, Melt Composition, Temperature and Pressure on the Oxidation State of Cerium in Silicate Melts. *Chemical Geology* **2014**, *366*, 52–60. https://doi.org/10.1016/j.chemgeo.2013.12.015.
(27) Mallmann, G.; Burnham, A. D.; Fonseca, R. O. C. Mineral-Melt Partitioning of Redox-Sensitive Elements. In *Magma Redox Geochemistry*; American Geophysical Union (AGU), 2021; pp 345–367. https://doi.org/10.1002/9781119473206.ch17.
(28) Burnham, A. D.; Berry, A. J. An Experimental Study of Trace Element Partitioning between Zircon and Melt as a Function of Oxygen Fugacity. *Geochimica et Cosmochimica Acta* **2012**, *95*, 196–212. https://doi.org/10.1016/j.gca.2012.07.034.
(29) Smythe, D. J.; Brenan, J. M. Cerium Oxidation State in Silicate Melts: Combined f O 2 , Temperature and Compositional Effects. *Geochimica et Cosmochimica Acta* **2015**, *170*, 173–187. https://doi.org/10.1016/j.gca.2015.07.016.
(30) Donatini, A.; Georges, P.; Fevre, T.; Cormier, L.; Neuville, D. R. Investigating Cerium Redox Changes between Aluminosilicate Glass and Melt: A Multispectroscopic Approach. *The Journal of Chemical Physics* **2024**, *160*, 124503.
(31) Vantelon, D.; Trcera, N.; Roy, D.; Moreno, T.; Mailly, D.; Guilet, S.; Metchalkov, E.; Delmotte, F.; Lassalle, B.; Lagarde, P.; Flank, A.-M. The LUCIA Beamline at SOLEIL. *J Synchrotron Rad* **2016**, *23* (2), 635–640. https://doi.org/10.1107/S1600577516000746.
(32) Baudelet, F.; Kong, Q.; Nataf, L.; Cafun, J. D.; Congeduti, A.; Monza, A.; Chagnot, S.; Itié, J. P. ODE: A New Beam Line for High-Pressure XAS and XMCD Studies at SOLEIL. *High Pressure Research* **2011**, *31* (1), 136–139. https://doi.org/10.1080/08957959.2010.532794.
(33) Hazemann, J.-L.; Proux, O.; Nassif, V.; Palancher, H.; Lahera, E.; Da Silva, C.; Braillard,

A.; Testemale, D.; Diot, M.-A.; Alliot, I.; Del Net, W.; Manceau, A.; Gélébart, F.; Morand, M.; Dermigny, Q.; Shukla, A. High-Resolution Spectroscopy on an X-Ray Absorption Beamline. *J Synchrotron Rad* **2009**, *16* (2), 283–292. https://doi.org/10.1107/S0909049508043768.
(34) Newville, M. Larch: An Analysis Package for XAFS and Related Spectroscopies. *J. Phys.: Conf. Ser.* **2013**, *430*, 012007. https://doi.org/10.1088/1742-6596/430/1/012007.
(35) Berry, A. J.; Stewart, G. A.; O'Neill, H. St. C.; Mallmann, G.; Mosselmans, J. F. W. A Re-Assessment of the Oxidation State of Iron in MORB Glasses. *Earth and Planetary Science Letters* **2018**, *483*, 114–123. https://doi.org/10.1016/j.epsl.2017.11.032.
(36) Wilke, M.; Farges, F.; Petit, P.-E.; Brown, G. E.; Martin, F. Oxidation State and Coordination of Fe in Minerals: An Fe K-XANES Spectroscopic Study. *American Mineralogist* **2001**, *86* (5–6), 714–730. https://doi.org/10.2138/am-2001-5-612.
(37) Neuville, D. R.; Hennet, L.; Florian, P.; De Ligny, D. In Situ High-Temperature Experiments. *Reviews in Mineralogy and Geochemistry* **2014**, *78* (1), 779–800. https://doi.org/10.2138/rmg.2013.78.19.
(38) Vercamer, V. Spectroscopic and Structural Properties of Iron in Silicate Glasses. *Thesis* **2016**, 100.
(39) Volotinen, T. T.; Parker, J. M.; Bingham, P. A. Concentrations and Site Partitioning of Fe2+ and Fe3+ Ions in a Soda–Lime–Silica Glass Obtained by Optical Absorbance Spectroscopy. *Physics and Chemistry of Glasses* **2008**, *49* (5).
(40) Cid-Aguilar, J. G.; Cabrera-llanos, Marcos Cabrera; Kiyama-Rodriguez. Colorless Glass Composition. US 2010/0297415 A1, November 25, 2010.
(41) Schreiber, H. D. Redox Processes in Glass-Forming Melts. *Journal of Non-Crystalline Solids* **1986**, *84* (1–3), 129–141. https://doi.org/10.1016/0022-3093(86)90770-2.
(42) Gueriau, P.; Mocuta, C.; Bertrand, L. Cerium Anomaly at Microscale in Fossils. *Anal. Chem.* **2015**, *87* (17), 8827–8836. https://doi.org/10.1021/acs.analchem.5b01820.
(43) Gonçalves Ferreira, P.; De Ligny, D.; Lazzari, O.; Jean, A.; Cíntora-González, O.; Neuville, D. R. Photoreduction of Iron by a Synchrotron X-Ray Beam in Low Iron Content Soda-Lime Silicate Glasses. *Chemical Geology* **2013**, *346*, 106–112. https://doi.org/10.1016/j.chemgeo.2012.10.029.
(44) Dickenson, M. P.; Hess, P. C. Redox Equilibria and the Structural Role of Iron in Alumino-Silicate Melts. *Contr. Mineral. and Petrol.* **1982**, *78* (3), 352–357. https://doi.org/10.1007/BF00398931.
(45) Sack, R. O.; Carmichael, I. S. E.; Rivers, M.; Ghiorso, M. S. Ferric-Ferrous Equilibria in Natural Silicate Liquids at 1 Bar. *Contr. Mineral. and Petrol.* **1981**, *75* (4), 369–376. https://doi.org/10.1007/BF00374720.
(46) Kress, V. C.; Carmichael, I. S. E. The Compressibility of Silicate Liquids Containing Fe203 and the Effect of Composition, Temperature, Oxygen Fugacity and Pressure on Their Redox States. *Contributions to Mineralogy and Petrology 108*, 82–92.
(47) Stabile, P.; Giuli, G.; Cicconi, M. R.; Paris, E.; Trapananti, A.; Behrens, H. The Effect of Oxygen Fugacity and Na/(Na+K) Ratio on Iron Speciation in Pantelleritic Glasses. *Journal of Non-Crystalline Solids* **2017**, *478*, 65–74. https://doi.org/10.1016/j.jnoncrysol.2017.09.051.
(48) Wilke, M.; Farges, F.; Partzsch, G. M.; Schmidt, C.; Behrens, H. Speciation of Fe in Silicate Glasses and Melts by In-Situ XANES Spectroscopy. *American Mineralogist* **2007**, *92* (1), 44–56. https://doi.org/10.2138/am.2007.1976.
(49) Giuli, G.; Paris, E.; Pratesi, G.; Koeberl, C.; Cipriani, C. Iron Oxidation State in the Fe- rich Layer and Silica Matrix of Libyan Desert Glass: A High- resolution XANES Study. *Meteorit & Planetary Scien* **2003**, *38* (8), 1181–1186. https://doi.org/10.1111/j.1945-5100.2003.tb00306.x.
(50) Paulose, P. I.; Jose, G.; Thomas, V.; Unnikrishnan, N. V.; Warrier, M. K. R. Sensitized FLuorescence of Ce3þ/Mn2þ System in Phosphate Glass. *Journal of Physics and Chemistry of Solids* **2003**, 6.
(51) Weyl, W. A.; Pincus, A. G.; Badger, A. E. Vanadium as a Glass Colorant. *J American Ceramic Society* **1939**, *22* (1–12), 374–377. https://doi.org/10.1111/j.1151-2916.1939.tb19483.x.
(52) Cook, G. B.; Cooper, R. F.; Wu, T. Chemical Diffusion and Crystalline Nucleation during Oxidation of Ferrous Iron-Bearing Magnesium Aluminosilicate Glass. *Journal of Non-Crystalline Solids* **1990**, *120* (1), 207–222. https://doi.org/10.1016/0022-3093(90)90205-Z.
(53) Stroud, J. S. Concentration Quenching of Nd^3+ Fluorescence. *Appl. Opt.* **1968**, *7* (5), 751. https://doi.org/10.1364/AO.7.000751.
(54) Herrmann, A.; Othman, H. A.; Assadi, A. A.; Tiegel, M.; Kuhn, S.; Rüssel, C. Spectroscopic Properties of Cerium-Doped Aluminosilicate Glasses. *Opt. Mater. Express, OME* **2015**, *5* (4), 720–732. https://doi.org/10.1364/OME.5.000720.
(55) Herrmann, A.; Fibikar, S.; Ehrt, D. Time-Resolved Fluorescence Measurements on Eu3+- and Eu2+-Doped Glasses. *Journal of Non-Crystalline Solids* **2009**, *355* (43–44), 2093–2101. https://doi.org/10.1016/j.jnoncrysol.2009.06.033.
(56) Chandrasekhar, S. Stochastic Problems in Physics and Astronomy. *Reviews of Modern Physics* **1943**, *15* (1), 1–89.
(57) Gómez-Salces, S.; Barreda-Argüeso, J. A.;

Valiente, R.; Rodríguez, F. Solarization-Induced Redox Reactions in Doubly Ce3+/Mn2+-Doped Highly Transmission Glasses Studied by Optical Absorption and Photoluminescence. *Solar Energy Materials and Solar Cells* **2016**, *157*, 42–47. https://doi.org/10.1016/j.solmat.2016.05.010.
(58) Trusova, E. E.; Bobkova, N. M.; Gurin, V. S.; Gorbachuk, N. I. Formation of Coloring Complexes in Glass Colored with Cerium and Titanium Oxides. *Glass Ceram* **2007**, *64* (9–10), 346–348. https://doi.org/10.1007/s10717-007-0086-4.
(59) Berry, A. J.; Shelley, J. M. G.; Foran, G. J.; O'Neill, H. St. C.; Scott, D. R. A Furnace Design for XANES Spectroscopy of Silicate Melts under Controlled Oxygen Fugacities and Temperatures to 1773 K. *J Synchrotron Rad* **2003**, *10* (4), 332–336. https://doi.org/10.1107/S0909049503007556.
(60) Paul, A. Oxidation-Reduction Equilibrium in Glass. *Journal of Non Crystalline Solids* **1990**, *123*, 354–362.
(61) Cooper, R. F. Redox Thermodynamics and Kinetics in Silicate Melts and Glasses. In *Encyclopedia of Glass Science, Technology, History, and Culture*; Richet, P., Conradt, R., Takada, A., Dyon, J., Eds.; Wiley, 2021; pp 581–596. https://doi.org/10.1002/9781118801017.ch5.6.
(62) Johnston, W. D. Oxidation-Reduction Equilibria in Molten Na2O.2SiO2 Glass. *Journal of the American Ceramic Society* **1965**, *48* (4), 184–190. https://doi.org/10.1111/j.1151-2916.1965.tb14709.x.